

# Journal of Biomedical Optics

[SPIEDigitalLibrary.org/jbo](http://SPIEDigitalLibrary.org/jbo)

## **Automatic characterization of neointimal tissue by intravascular optical coherence tomography**

Giovanni J. Ughi  
Kristin Steigerwald  
Tom Adriaenssens  
Walter Desmet  
Giulio Guagliumi  
Michael Joner  
Jan D'hooge

# Automatic characterization of neointimal tissue by intravascular optical coherence tomography

Giovanni J. Ughi,<sup>a</sup> Kristin Steigerwald,<sup>b</sup> Tom Adriaenssens,<sup>a</sup> Walter Desmet,<sup>a</sup> Giulio Guagliumi,<sup>c</sup> Michael Joner,<sup>b</sup> and Jan D'hooge<sup>a</sup>

<sup>a</sup>University Hospitals Leuven, Department of Cardiovascular Diseases, and KU Leuven, Department of Cardiovascular Sciences, Herestraat 49, B3000 Leuven, Belgium

<sup>b</sup>Deutsches Herzzentrum and Technische Universität Munich, Medizinische Klinik, Klinikum rechts der Isar, Lazarettstraße 36, 80636 Munich, Germany

<sup>c</sup>Ospedale Papa Giovanni XXIII, Cardiovascular Department, Bergamo, Piazza OMS 1, 24100, Italy

**Abstract.** Intravascular optical coherence tomography (IVOCT) is rapidly becoming the method of choice for assessing vessel healing after stent implantation due to its unique axial resolution  $<20\ \mu\text{m}$ . The amount of neointimal coverage is an important parameter. In addition, the characterization of neointimal tissue maturity is also of importance for an accurate analysis, especially in the case of drug-eluting and bioresorbable stent devices. Previous studies indicated that well-organized mature neointimal tissue appears as a high-intensity, smooth, and homogeneous region in IVOCT images, while lower-intensity signal areas might correspond to immature tissue mainly composed of acellular material. A new method for automatic neointimal tissue characterization, based on statistical texture analysis and a supervised classification technique, is presented. Algorithm training and validation were obtained through the use of 53 IVOCT images supported by histology data from atherosclerotic New Zealand White rabbits. A pixel-wise classification accuracy of 87% and a two-dimensional region-based analysis accuracy of 92% (with sensitivity and specificity of 91% and 93%, respectively) were found, suggesting that a reliable automatic characterization of neointimal tissue was achieved. This may potentially expand the clinical value of IVOCT in assessing the completeness of stent healing and speed up the current analysis methodologies (which are, due to their time- and energy-consuming character, not suitable for application in large clinical trials and clinical practice), potentially allowing for a wider use of IVOCT technology. © 2014 Society of Photo-Optical Instrumentation Engineers (SPIE) [DOI: 10.1117/1.JBO.19.2.021104]

Keywords: optical coherence tomography; tissue characterization; stent; intravascular; image analysis; texture analysis.

Paper 130243SSR received Apr. 15, 2013; revised manuscript received Jun. 4, 2013; accepted for publication Jun. 18, 2013; published online Jul. 24, 2013.

## 1 Introduction

Intravascular optical coherence tomography (IVOCT) is increasingly used for assessing safety and efficacy of intracoronary devices, including newer generations of drug-eluting stents (DES) and bioresorbable vascular scaffolds.<sup>1,2</sup> Due to its excellent axial resolution ( $<20\ \mu\text{m}$ ), IVOCT allows for the accurate quantification of neointimal coverage on a strut level. This is of high importance as it was previously shown that the lack of coverage may be a potential predictor of late DES thrombosis.<sup>3,4</sup> However, this is not the only parameter that needs to be assessed. Recent studies pointed to the fact that IVOCT analysis should also take into consideration neointimal tissue differentiation (e.g., endothelium, smooth muscle cells [SMCs], and extracellular matrix),<sup>5,6</sup> suggesting that IVOCT is capable of defining “normal” and “abnormal” neointimal tissue based on its visual appearance. It was recognized earlier that well-organized mature tissue appears as a high-intensity, smooth, and homogeneous region in IVOCT images, while a lower-intensity signal might correspond to acellular material (i.e., proteoglycan or fibrin).<sup>7,8</sup> Another recent investigation provided the histological evidence that IVOCT is capable of characterizing neointimal tissue as described above and suggested that it is possible to differentiate such tissue into “mature” and “immature.”<sup>9</sup>

Mature tissue was characterized histologically as neointimal tissue predominantly composed of SMCs. In contrast, immature tissue was characterized as proteoglycan/collagen-rich neointimal tissue with few interdispersed SMCs.<sup>9</sup> Moreover, mature neointimal tissue was characterized by a minimal presence of RAM-11–positive macrophages in contrast to immature tissue.<sup>9</sup> Since the presence of immature neointimal tissue has been indicated as an important predictor of late stent thrombosis (LST) in human autopsies,<sup>10</sup> the distinction between mature and immature neointimal tissues could serve as surrogate for the assessment of vascular healing after stent implantation and thus (potentially) being of clinical importance. As such, in a future perspective, this holds potential for the identification of patients at risk for LST and thus for the adjustment of antiplatelet therapy to the patient needs (i.e., prolong if immature tissue exists).<sup>9,11</sup>

Currently, IVOCT analysis is performed by a very time-consuming manual procedure based on the qualitative assessment of image features, like low-intensity areas around the stent struts. This procedure is impractical for evaluating stents in the context of large clinical trials, where the number of inclusions may be limited by a long analysis time, and for clinical practice. Individual stent struts need to be analyzed one by one on a large number of consecutive frames resulting in a very cumbersome procedure.<sup>5,11</sup> Given that state-of-the-art IVOCT systems are able to acquire data with a very high frame rate (e.g., a single

Address all correspondence to: Giovanni J. Ughi, Massachusetts General Hospital, Wellman Center for Photomedicine, 40 Blossom Street, Boston, Massachusetts 02114. Tel: (617) 505 8880; E-mail: [gughi@mgh.harvard.edu](mailto:gughi@mgh.harvard.edu)

IVOCT dataset is usually composed of ~300 to 500 images, according to pullback speed and exact system specifics), the analysis of an entire stent may require a workload of 5 h or longer,<sup>12</sup> as thousands of struts need to be analyzed. Moreover, manual analysis is intrinsically subject to inter- and intra-server variability.

The aim of the present study was to develop a novel method for the automatic analysis of neointimal tissue. Such a quantitative and automated procedure would potentially allow for a more time-efficient and objective analysis of IVOCT data. It is important to notice that the final aim of the proposed method is the characterization of neointimal tissue healing, differentiating “mature” from “immature” neointimal tissue, which was shown to be a potential predictor of late stent-failure events such as stent thrombosis and restenosis.<sup>9</sup> Hereto, we proposed a tissue characterization algorithm based on supervised classification and statistical texture analysis. Algorithm training and validation were obtained through the use of 53 IVOCT images supported by histological data from atherosclerotic New Zealand White rabbits.<sup>9</sup> As such, automated analysis of neointimal tissue is achieved. Moreover, by combining this tissue characterization algorithm with a method for automatic stent strut segmentation recently proposed by our research group,<sup>13</sup> automatic analysis of neointimal tissue over an entire IVOCT pullback (thus over an entire stent) can potentially be fulfilled. This may allow for a time-efficient and systematic three-dimensional (3-D) analysis of IVOCT data, aiming to speed up current methodologies. As such, as a future perspective, automatic analysis of neointimal tissue may contribute for a better integration of this imaging modality in cardiovascular research and clinical practice.

## 2 Methods

The proposed algorithm consists of two main steps. First, statistical textural properties of IVOCT images are quantified; subsequently, a supervised classification algorithm is applied. The final aim is to generate a tissue-map, automatically depicting mature and immature tissues superimposed to the IVOCT images. Regions of interest (ROIs) for neointimal tissue analysis can be traced manually (semi-automatic approach), or automatically by means of methods for lumen and stent struts segmentation previously developed by our research group.<sup>13,14</sup>

### 2.1 Texture Analysis

Prior studies showed that statistical texture analysis can be successfully applied to OCT images for a reliable classification of different tissues.<sup>15</sup> Overall, a large number of textural features were described in literature.<sup>16–18</sup> A common challenge in the development of algorithms for tissue characterization is the identification of a subset of features able to optimally quantify the properties of the tissue being analyzed (i.e., a feature selection study). Starting from a total of 29 different statistical features, quantified over the training-set images (Sec. 4) by the use of image histogram (first-order statistics) and gray-level co-occurrence matrices (GLCM, second-order statistics),<sup>18</sup> feature selection was obtained by means of a state-of-the-art algorithm called minimum redundancy maximum relevance feature selection (mRMR).<sup>19</sup> In brief, mutual information between features is used to find the best feature “subspace” for optimal classification. It was shown that this feature selection scheme can be successfully applied to supervised classification problems.<sup>20</sup> Specific details about mRMR can be found in its original report.<sup>19</sup> Based on this process, a total of 12 different features

were retained: mean and kurtosis (first-order statistics), maximum probability, contrast, cluster prominence, cluster shade, correlation, homogeneity, sum of entropy, information measure of correlation, sum of variance, and difference entropy (second-order statistics). The specific formulas used to compute the selected features are reported in Table 1. The principle behind the use of GLCM is that not only do absolute pixel intensity levels need to be considered but also the relationships between adjacent pixels have to be quantified. As an example, GLCM contrast returns a measure of the intensity contrast between a pixel and its neighbors, over the whole image or ROI, independent from the absolute intensity values of pixels under evaluation.

### 2.2 Supervised Pixel Classification

Above-selected textural features were used to achieve a supervised pixel classification through a recently proposed algorithm: random forests (RF).<sup>21</sup> In brief, the main idea of RF is combining a large number of weak classifiers (i.e., binary trees) to achieve accurate classification results (averaging classifier). Each pixel to be classified is processed by multiple binary tree predictors where each tree is constituted by a subset of features of the training set. Every tree votes for a specific class and RF chooses the final result as the class with the larger number of votes. The principle behind this classification technique is that the correlation between individual base learners is reduced by choosing multiple predictors in a random subspace of the training data. Although this may be a counterintuitive procedure, it was shown that if the number of trees is large enough, RF can achieve robust classification with respect to noise and overfitting.<sup>21</sup> Classification parameters are the number of trees to grow (*n<sub>tree</sub>*) and the number of variables randomly sampled at each node (*n<sub>rand</sub>*). The reader is referred to the RF original report<sup>21</sup> and subsequent publications<sup>22</sup> for additional details.

To conclude the classification procedure, analyzed pixels are color-coded generating a tissue color-map able to clearly depict mature and immature neointimal tissues. It is important to notice that through this procedure each individual pixel is considered to be an independent observation and it is classified as “mature” or “immature” tissue. Results are finally scan-converted to standard IVOCT (Cartesian) domain for visualization purposes.

### 2.3 Implementation Details

Feature extraction and classification algorithms were applied to raw-data (polar domain) 16-bit images with a pixel dimension of 504 (number of A-scan lines) and 976 (pixels per A-scan line). All codes were implemented in Matlab® R2011a (MathWorks, Massachusetts), while the scan-conversion algorithm was implemented in C++ (Microsoft, Washington) as previously described<sup>13,23</sup> and executed in Matlab by means of the MEX libraries (MathWorks). Feature selection algorithm was applied using the original code (Matlab, MEX libraries, and C++), made freely available for download on the mRMR authors’ website.<sup>19,24</sup>

Computation times were quantified on a laptop computer with an i7-3720QM processor (Intel Corporation, California), 16 GB of RAM memory, and a Quadro k2000M video card (NVIDIA Corporation, California) running a 64-bit OS (Windows 7, Microsoft).

**Table 1** Mathematical definitions of first- and second-order statistical features used in this study.

<b>Histogram: First-order image stat.</b>	$p(i) = H(i)/N$ with $i = 1, \dots, G$	- $H(i)$ (image histogram) a function indicating the number of pixels with intensity $i \forall i$
Mean	$\mu = \sum_{i=1}^G i \cdot p(i)$	- $N$ the total number of pixels
Kurtosis	$\sigma^{-4} \sum_{i=1}^G (i - \mu)^4 p(i) - 3$	- $G$ the total number of int. levels appearing in the image
<b>Co-occurr. prob.: Second-order image stat.</b>	$C_{ij} = \frac{P_{ij}}{\sum_{i=1}^G P_{ij}}$	- with $\sigma$ (first-order variance): $\sigma^2 = \sum_{i=1}^G (i - \mu)^2 p(i)$
Max. Probab.	$\max\{C_{ij}\}$	Where $P_{i,j}$ represents the number of occurrences of gray levels $i$ and $j$ for a certain $(d, \theta)$ pair in a given region
Contrast	$\sum C_{ij}(i - j)^2$	with $\sum = \sum_{i=1}^G \sum_{j=1}^G$
Cluster prominence	$\sum C_{ij}(i + j - \mu_i - \mu_j)^4$	$\mu_i = \sum i C_{ij}$ $\mu_j = \sum j C_{ij}$
Cluster shade	$\sum C_{ij}(i + j - \mu_i - \mu_j)^3$	
Correlation	$\sum \frac{(i - \mu_i)(j - \mu_j) \cdot C_{ij}}{\sigma_i \sigma_j}$	$\sigma_i = \sum [(i - \mu_i)^2]^{0.5}$ $\sigma_j = \sum [(j - \mu_j)^2]^{0.5}$
Homogeneity	$\sum \frac{C_{ij}}{1 +  i - j }$	
Sum of entropy (se)	$-\sum_{i=2}^{2G} p_{i+j}(i) \log(p_{i+j}(i) + eps)$	$p_{i+j} = \sum_{i+j=k} C_{ij}$ with $k = 2, 3, \dots, G$
Sum of variance	$\sum_{i=2}^{2G} (i - se)^2 p_{i+j}(i)$	
Information measures of correlation*	$\{1 - \exp[-2(h_{ij2} - h_{ij})]\}^{1/2}$	$h_{ij} = -\sum C_{ij} \log(C_{ij} + eps)$ $h_{ij2} = -\sum p_i p_j \log(p_i p_j + eps)$ $p_i = \sum_i C_{ij}$ & $p_j = \sum_j C_{ij}$
Difference entropy*	$-\sum_{i=1}^G p_{i-j}(i) \log(p_{i-j}(i) + eps)$	$p_{i-j} = \sum_{ i-j =k} C_{ij}$ with $k = 1, 2, \dots, G$

\*eps is an arbitrarily small constant equal to  $2^{-52}$  (floating point accuracy).

### 2.3.1 Algorithm parameters

Parameters for textural features quantification were empirically selected to be  $K = 7$  pixels (squared kernel),  $G = 64$  (number of gray levels for image quantization), and  $d = 2$  (pixel distance) aiming for best visual separability between the two classes (assessed on the training-set images). GLCM computation angles were selected to be  $\theta = 0, 45, 90,$  and  $135$  deg, including all the four possible directions for GLCM quantifications. Subsequently, RF's parameters were empirically selected to be  $n_{tree} = 120$  and  $n_{rand} = 10$  by testing a wide range of different values trying to minimize RF computational time without limiting classification accuracy.

## 3 Experimental Data

A total of 53 pairs of IVOCT images and histological slices were used in this study. An atherosclerotic rabbit model of iliac artery stenting was used to obtain different types of neointimal tissue

as detailed in a previous study.<sup>9</sup> In brief, images were collected from both DES and bare-metal stents (BMS) after 28 and 42 days of stent implantation. A total of 14 atherosclerotic New Zealand White rabbits received everolimus eluting stents ( $n = 5$ , Xience, Abbott Laboratories, Illinois), zotarolimus-eluting stents ( $n = 5$ , Resolute, Medtronic, Minnesota), and BMS ( $n = 4$ , Driver, Medtronic). IVOCT data were acquired *in situ* (arteries remaining in place) immediately after euthanasia utilizing a commercial IVOCT system (C7-XR™ imaging system and Dragonfly™ catheters, St. Jude, St. Paul, Minnesota). A default pullback speed of 20 mm/s (100 frames/s) during flush with contrast media for removing residual blood was used.

For histopathological analyses, excised vessels were embedded in methylmethacrylate plastic. Histological slices were stained with hematoxylin and eosin and Movat pentachrome and additionally stained for fibrin (Carstairs stain), SMCs (alpha-SM-actin immunostaining), and macrophages (RAM-11 immunostaining). Histology cross-sections were analyzed by

two independent pathologists and there was 100% concordance with respect to the judgment of mature versus immature tissue by histology. Subsequently, IVOCT frames were coregistered to histological cross-sections as follows: for every stent, approximately eight to nine histological sections were cut. Using stent edges as spatial references, histological cross-sections were matched to IVOCT images. However, in case a full and correct 1:1 registration of all individual stent struts was not feasible (e.g., due to multiple factors such as different cutting angle between histology and IVOCT and IVOCT longitudinal sampling), images were discarded. Similarly, cross-sectional images not presenting enough neointimal coverage for tissue analysis were also removed. This procedure resulted in a total of 53 pairs of IVOCT and histology cross-sectional images meeting the criteria above, allowing to assess neointimal tissue in three to four different sections of each stent (e.g., proximal, middle, and distal). Given that all sections were taken from different spatial positions or different vessels, such selection procedure ensured the creation of two independent sets of images for training and validation, as it is requested for the correct evaluation of the performances of any classification algorithm. To conclude this procedure, 95 ROIs were manually traced on the IVOCT images according to histopathological analyses, resulting in a total of 42 and 53 ROIs of mature and immature tissues, respectively. Please note that pathologists were blinded to automatic IVOCT analysis in order to avoid bias.

#### 4 Training and Validation

The algorithm training set was created by arbitrarily selecting 20 of the 53 IVOCT images paired with histology. A balanced training set including  $\sim 10^4$  observations (i.e., image pixels) was created over a total of 23 tissue ROIs (11 mature and 12 immature). The remaining 33 images were used for the creation of the testing set. Overall, 72 ROIs were traced by the pathologist on these images incorporating a total of 31 and 41 mature and immature ROIs, respectively, including approximately  $1.2 \times 10^5$  testing pixels. A description of this dataset and the creation of the training and testing sets are illustrated in Fig. 1.

Validation results were quantified in terms of pixel-wise classification accuracy, as typically done in classification problems.<sup>25</sup> A one-to-one correspondence for every pixel automatically classified and “IVOCT histology assessment” was created. Both global and per-class pixel-wise accuracies were considered. Such accuracies were computed using standard formulae commonly accepted in medical literature:<sup>26</sup>

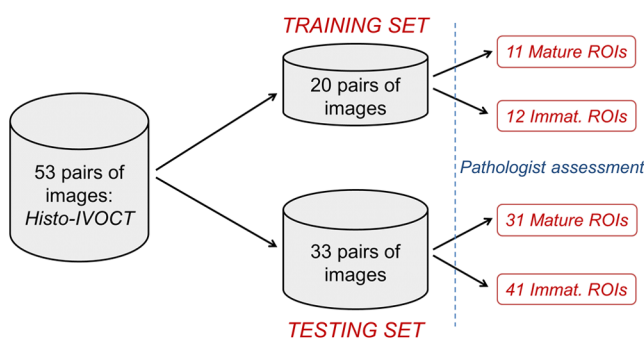


**Fig. 1** Creation of the dataset and subsequent composition of the algorithm training and testing sets.

$$\text{Accuracy} = \frac{[\text{Number of correct decisions}]}{[\text{Number cases}]}$$

Furthermore, algorithm accuracy in terms of “two-dimensional (2-D) region assessment” was evaluated by making automatically classified ROIs uniform, according to the majority of pixels belonging to a specific class (e.g., a region showing 85% mature and 15% immature tissue pixels was thus classified as a “mature” ROI). This allowed for an accurate comparison of automated results to histological analysis, as the pathologist traced ROIs of uniform tissue over IVOCT images. Such an additional region-based 2-D validation is reported in terms of accuracy, sensitivity, specificity, positive predictive value (PPV), and negative predictive value (NPV). Values were computed as follows:<sup>26</sup>

$$\text{Sensitivity} = \frac{[\text{Number of True Positive Decisions}]}{[\text{Number of Actually Positive Cases}]}$$

$$\text{Specificity} = \frac{[\text{Number of True Negative Decisions}]}{[\text{Number of Actually Negative Cases}]}$$

$$\text{PPV} = \frac{[\text{Number of False Positive Decisions}]}{[\text{Number of Actually Negative Cases}]}$$

$$\text{NPV} = \frac{[\text{Number of Negative Decisions}]}{[\text{Number of Actually Positive Cases}]}$$

#### 5 Results

Figures 2 and 3 represent examples of automatic tissue characterization. From the figures it is possible to appreciate the different IVOCT appearance of mature and immature neointimal tissues and automatic analysis results. Table 2 reports measured values of the statistical textural features for mature and immature neointimal tissues, respectively.

Overall, a total of  $\sim 1.2 \times 10^5$  pixels were taken into account by this validation procedure. Pixel-wise classification accuracy, over the 33 images composing the algorithm testing set, resulted to be 87% with a per-class accuracy of 83% for mature and 90% for immature tissues.

Subsequent 2-D region-based validation (over 72 ROIs) resulted in a global accuracy of 92%, sensitivity of 91%, specificity of 93% with PPV and NPV of 95% and 87%, respectively.

Computational time for a sample of  $10^3$  pixels was 13 s (on average) for texture analysis (including both co-occurrence matrix creation and statistical features quantification), while a computational time of 6 s was found for RF classification.

#### 6 Discussion

An algorithm for automatic, quantitative, and therefore time-efficient characterization of neointimal tissue by IVOCT data was presented. Algorithm validation was obtained by comparing automatic IVOCT classification to correspondent histology (gold standard) for a total of 72 ROIs over 33 IVOCT-histological paired images, located by an independent pathologist blinded to the algorithm results to avoid bias. High-accuracy

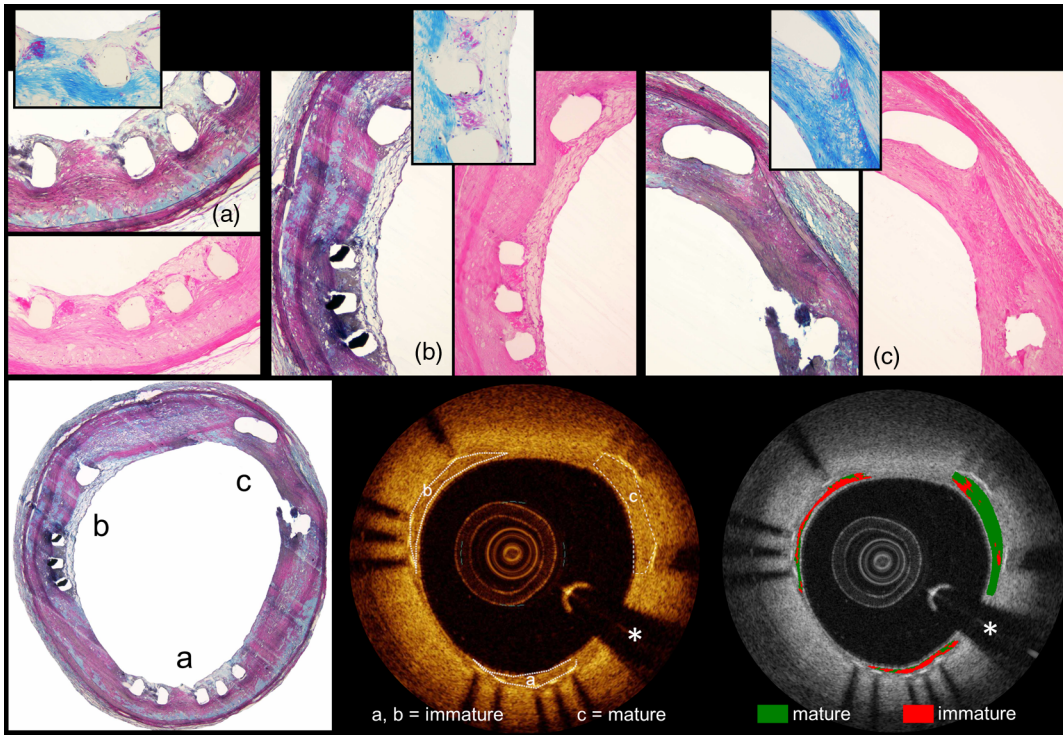


**Fig. 2** Examples of histological cross-sections (bottom-left image) showing both immature [(a), (b)] and mature (c) neointimal tissue over the stent strut surface. Subimages (a) stained by Movat pentachrome (upper image) and hematoxylin and eosin (lower image) and (b) represent immature tissue. Inlets show images after Carstairs stain to detect fibrin (pink color). Panel (c) represents mature tissue in the absence of fibrin (inlet) and presence of smooth muscle cells and proteoglycans after Movat pentachrome and hematoxylin and eosin staining. Two independent pathologists blinded to automatic classification results manually traced three ROIs on the IVOCT image (bottom-center image) according to corresponding histological assessment. Bottom-right figure shows the automatic tissue characterization results. Mature tissue is automatically depicted in green and immature tissue is depicted in red. The white asterisk (\*) indicates the guide-wire shadowing artifact.

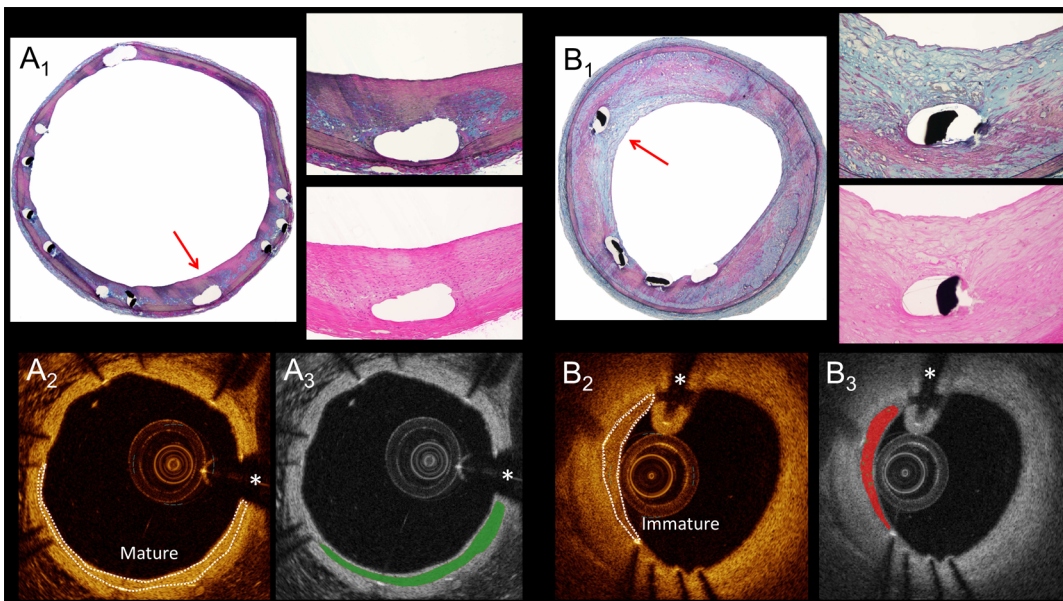


**Fig. 3** Image (a1) shows an example of mature neointimal tissue while image (b1) shows an example of immature neointimal tissue (Movat pentachrome and hematoxylin and eosin stains). Magnifications of mature and immature neointimal tissues are displayed on one side (red arrows indicate the two regions that are magnified). ROIs (images a2 and b2) were traced by two independent pathologists over stent strut surface blinded to algorithm automatic results to avoid bias. Images a3 and b3 show the final results of automatic tissue classification. Mature tissue is depicted in green, immature tissue is depicted in red, and the white asterisk (\*) indicates the guide-wire shadowing artifact.

**Table 2** Measured values of the statistical features used in this study quantified over the two different tissue types.

	Mature	Immature		Mature	Immature
<b>First-order stat.</b>			Cluster shade	$1.1 \pm 2.2 \cdot 10^3$	$1.2 \pm 2.9 \cdot 10^2$
Mean	$20.4 \pm 5.0$	$8.4 \pm 2.9$	Correlation	$-3.4 \pm 2.6 \cdot 10^{-2}$	$-3.8 \pm 2.5 \cdot 10^{-2}$
Kurtosis	$2.8 \pm 0.8$	$3.2 \pm 1.2$	Homogeneity	$9.1 \pm 4.6 \cdot 10^{-2}$	$22.2 \pm 9.0 \cdot 10^{-2}$
<b>Second-order stat.</b>			Sum of entropy	$3.1 \pm 0.2$	$2.6 \pm 0.3$
Max. Prob.	$4.2 \pm 1.5 \cdot 10^{-2}$	$7.0 \pm 2.6 \cdot 10^{-2}$	Sum of variance	$1.8 \pm 0.9 \cdot 10^3$	$0.3 \pm 0.2 \cdot 10^3$
Contrast	$216 \pm 125$	$37 \pm 34$	Inf. meas. of correlation	$99 \pm 1 \cdot 10^{-2}$	$94 \pm 5 \cdot 10^{-2}$
Cluster prominence	$1.5 \pm 1.9 \cdot 10^5$	$6.4 \pm 1.4 \cdot 10^3$	Diff. entropy	$2.8 \pm 0.2$	$2.1 \pm 0.3$

NOTE: Values are reported as mean  $\pm$  standard deviation.

values were observed (i.e., accuracy of 92% with both specificity and sensitivity  $>90\%$ ) when comparing automatic results over 2-D regions, suggesting that automatic IVOCT analysis can correctly differentiate neointimal tissue composition. Given that the testing set was created by images acquired through a commercial IVOCT system, this algorithm may be directly applied to *in vivo* datasets. This would be important for a better integration of IVOCT in cardiovascular research and clinical practice, especially when IVOCT is used to assess vessel reaction to stent implantation (e.g., DES and bioresorbable stents) as a marker of device safety and efficacy.

### 6.1 Validation

In the present study, neointimal tissue characterization was applied to specific ROIs located by an independent pathologist on the basis of histological assessment. The algorithm accuracy was quantified both on a pixel-wise and on a regional manner. Although histology is able to provide tissue details on a micrometer level, this cannot be directly translated to individual IVOCT image pixels due to different image resolution ( $\sim 15 \mu\text{m}$ ). As such, pathologists usually had to depict over IVOCT data homogeneous regions of tissue (i.e., ignoring minimal variations of tissue type) on the basis of corresponding histological analysis. Therefore, 2-D regional validation was also reported in this study in order to give more complete information about the algorithm accuracy.

It is important to notice that pathologists were blinded to algorithms results in order to avoid bias. Moreover, bias was further reduced as “mature” and “immature” tissue ROIs were defined only on the basis of histological analysis without considering IVOCT image appearance. In addition, the images included in both the training and testing sets were selected to be uncorrelated from each other (given that they were extracted from different spatial positions and vessels), thus generating two sets of images that are completely independent from each other as it is requested for a correct validation of the proposed algorithm. In any case, it is worth mentioning that during histological analysis also, tissue that was not possible to classify itself as mature or immature was occasionally found. This type of tissue was excluded from further analysis as it was beyond the scope of this study.

### 6.2 Classification

Overall, two optical properties (i.e., scattering and attenuation) can be used for tissue analysis by means of IVOCT.<sup>27</sup> However, for the issue addressed in this study, only tissue backscattering gave important information about neointimal tissue composition. As a matter of fact, qualitative analysis of mature and immature tissues over IVOCT images (as indicated by histology) revealed that both these tissue types present a low attenuation coefficient (Figs. 2 and 3).<sup>8</sup> Although tissue attenuation was not systematically quantified over the training set data (this may be obtained through the use of recently proposed methods for IVOCT attenuation estimation<sup>28</sup>), it is unlikely that attenuation can be a valid discriminant between mature and immature neointimal tissues as also suggested by an earlier study.<sup>8</sup> As such, we proposed the use of statistical texture analysis in order to quantify critical information on tissue backscattering, i.e., quantifying the stochastic behavior of the backscatter process by quantifying the spatial distribution of the individual scattering sites, as qualitative properties that experts use to manually classify neointimal tissue.<sup>7,8</sup> In this regard, both first- (image histogram) and second-order statistical features (GLCM) were taken into account for achieving an accurate classification of neointimal tissue. As a matter of fact, the use of GLCM provided important and additional information for neointimal tissue classification (e.g., tissue-specific speckle appearance<sup>15</sup>) as it considers not only absolute intensity levels but also the relationship between the values of adjacent pixels (e.g., mature neointimal tissue was described to present not only higher intensity values with respect to immature tissue but also a more homogeneous appearance<sup>7,8</sup>).

With respect to the classification algorithm, the selection of RF was driven by its specific properties. First, RF presents comparable accuracy to other state-of-the-art methods (i.e., support vector machines) for image classification problems.<sup>29</sup> Second, RF presents reduced computational times, making it suitable for the online analysis of large samples of data (e.g., image pixels) as required by this study. Despite these considerations, a quantitative comparison between multiple classifiers (which was beyond the scope of the current study) may lead to the selection of the best classifier for the optimal balance between classification accuracy and computational time.

### 6.3 Limitations and Further Improvements

Although the use of second-order statistical features (i.e., co-occurrence matrices), quantifying the relationship between intensity levels of different pixels rather than absolute gray levels, may address undesired changes in image intensity (e.g., due to eccentric IVOCT catheter position), it is worth mentioning that additional developments of the proposed algorithm taking into account additional effects related to IVOCT image acquisition (e.g., image point spread function and confocal properties of the imaging catheter<sup>30</sup>) may further increase the classification accuracy. Moreover, it has to be noticed that in case of image artifacts seriously compromising image quality (e.g., incomplete blood flushing, blood in the catheter, stent strut saturation artifact<sup>1,5</sup>), both qualitative (i.e., manual) and quantitative neointimal tissue analysis may present a limited accuracy and in some cases be unreliable. It is also important to notice that, due to intrinsic properties of IVOCT technology, a reliable assessment of neointimal tissue requires a layer of minimum thickness  $\approx 45 \mu\text{m}$ .

In addition, our research group recently focused on the development and validation of various algorithms for the automatic 3-D segmentation and visualization of IVOCT datasets.<sup>13,14,31</sup> The combination of 3-D stent segmentation to the algorithm proposed in this study would be a natural extension potentially capable of achieving a fully automatic assessment of neointimal tissue over the entire IVOCT pullback and thus over an entire stent (3-D analysis). More in detail, ROIs can be automatically located starting from stent strut and lumen segmentation. Although such structures can be automatically segmented,<sup>13</sup> it is important to notice that in case of suboptimal image quality (i.e., artifacts), a limited number of manual corrections may be needed. Anyway, such automatic identification of image ROIs may allow for a successful automatic and, thus, time-efficient analysis of neointimal tissue through an entire IVOCT dataset. Nevertheless, this approach was not evaluated in this study, as a correct validation would require histological slices of the entire vessel (which are not currently available) and automatically traced ROIs may not necessarily correspond to those blindly traced by the pathologists. However, validation results suggested that a reliable automatic analysis of neointimal tissue over the stent surface can potentially be achieved through the proposed method. Moreover, implementation of the proposed algorithm in a faster language (e.g., graphics processing unit parallel processing) may potentially allow for a (close to) real-time analysis of entire IVOCT datasets.

### 6.4 Neointimal Tissue Analysis

In this study, an automated classification framework for mature and immature neointimal tissue healing was proposed. The final aim of this project was to achieve an (automatic) early discrimination of immature tissue, as it was suggested to be a potential predictor of late stent failure events, such as stent neoatherosclerosis, restenosis, and thrombosis.<sup>9</sup>

As a matter of fact, mature tissue was indicated as surrogate for well-healed neointima, while immature tissue was related to delayed neointimal healing that could put the patient at risk for LST when discontinuing antiplatelet therapy. As such, this holds potential for the identification of patients at risk for LST and potentially being of help adjusting antiplatelet therapy to the patient needs (i.e., prolong if immature tissue exists).<sup>9,11</sup>

Furthermore, the automated and quantitative analysis framework described in this study may be applied for core lab analysis investigating safety and efficacy of novel stent devices and, in a future perspective, improving current therapies.

## 7 Conclusion

A novel method for the automatic characterization of neointimal tissue covering stents by IVOCT was presented. The algorithm validation was obtained through the use of histology as ground truth, showing high-accuracy values. This holds potential for a better integration of IVOCT in clinical practice as a diagnostic tool and in cardiovascular research for the development of novel devices and therapies for the treatment of atherosclerosis.

### Acknowledgments

This work was supported by the Research Foundation Flanders (FWO—Grant No. G.0690.09N), Industrial Research Foundation KU Leuven (IOF—Grant No. ZKC2992), and the European Union under the Seventh Framework Programme (FP7, PRESTIGE—Grant No. 260309). Tom Adriaenssens is also supported by a clinical doctoral grant of the FWO. Dr. G. Guagliumi received consulting fees from Boston Scientific and St. Jude Medical and grant support from Abbot Vascular, Boston Scientific, and St. Jude Medical.

### References

1. G. Tearney et al., "Consensus standards for acquisition, measurement, and reporting of intravascular optical coherence tomography studies," *J. Am. Coll. Cardiol.* **59**(12), 1058–1072 (2012).
2. S. Brugaletta et al., "Circumferential evaluation of the neointima by optical coherence tomography after ABSORB bioresorbable vascular scaffold implantation: can the scaffold cap the plaque?," *Atherosclerosis* **221**(1), 106–112 (2012).
3. A. V. Finn et al., "Pathological correlates of late drug-eluting stent thrombosis: strut coverage as a marker of endothelialization," *Circulation* **115**(18), 2435–2441 (2007).
4. G. Guagliumi et al., "Examination of the in vivo mechanisms of late drug-eluting stent thrombosis: findings from optical coherence tomography and intravascular ultrasound imaging," *J. Am. Coll. Cardiol. Interv.* **5**(1), 12–20 (2012).
5. H. G. Bezerra et al., "Intracoronary optical coherence tomography: a comprehensive review," *J. Am. Coll. Cardiol. Interv.* **2**(11), 1035–1046 (2009).
6. C. Templin et al., "Coronary optical frequency domain imaging (OFDI) for in-vivo evaluation of stent healing: comparison with light and electron microscopy," *Eur. Heart J.* **31**(14), 1792–1801 (2010).
7. G. F. Attizzani and H. G. Bezerra, "Contemporary assessment of stent strut coverage by OCT," *Int. J. Cardiovasc. Imag.* **29**(1), 23–27 (2013).
8. T. Teramoto et al., "Intriguing peri-strut low intensity area detected by optical coherence tomography after coronary stent deployment," *Circ. J.* **74**(6), 1257–1259 (2010).
9. C. Malle et al., "Tissue characterization after DES implantation utilizing optical coherence tomography," *Arterioscler. Thromb. Vasc. Biol.* **33**(6), 1376–1383 (2013).
10. M. Joner et al., "Pathology of drug-eluting stents in humans: delayed healing and late thrombotic risk," *J. Am. Coll. Cardiol.* **48**(1), 193–202 (2006).
11. T. Kubo et al., "Application of optical coherence tomography in percutaneous coronary intervention," *Circ. J.* **76**(9), 2076–2083 (2012).
12. T. Okamura, "Stent evaluation using three dimensional optical coherence tomography," 2010, [http://www.summitmd.com/pdf/pdf/1430\\_Safety\\_4\\_TakayukiOkamura.pdf](http://www.summitmd.com/pdf/pdf/1430_Safety_4_TakayukiOkamura.pdf) (March 2013).
13. G. J. Ughi et al., "Automatic segmentation of in-vivo intra-coronary optical coherence tomography images to assess stent strut apposition and coverage," *Int. J. Cardiovasc. Imag.* **28**(2), 229–241 (2012).

14. G. J. Ughi et al., "Automated volumetric stent analysis of in-vivo intracoronary optical coherence tomography three-dimensional datasets," *Proc. SPIE* **8091**, 809110 (2011).
15. K. W. Gossage et al., "Texture analysis of optical coherence tomography images: feasibility for tissue classification," *J. Biomed. Opt.* **8**(3), 570–575 (2003).
16. A. Haralick, K. Shanmugam, and I. Dinstein, "Texture features for image classification," *IEEE Trans. Syst. Man. Cybern.* **3**(6), 610–621 (1973).
17. D. A. Clausi, "An analysis of co-occurrence texture statistics as a function of gray level quantization," *Can. J. Rem. Sens.* **28**(1), 45–62 (2002).
18. A. Materka and M. Strzelecki, "Texture analysis methods—A review," 1998, [http://www.elel.p.lodz.pl/programy/cost/pdf\\_1.pdf](http://www.elel.p.lodz.pl/programy/cost/pdf_1.pdf) (April 2013).
19. H. Peng, F. Long, and C. Ding, "Feature selection based on mutual information: criteria of max-dependency, max-relevance, and min-redundancy," *IEEE Trans. Pattern Anal. Mach. Intell.* **27**(8), 1226–1238 (2005).
20. C. Ding and H. Peng, "Minimum redundancy feature selection from microarray gene expression data," *J. Bioinform. Comput. Biol.* **3**(2), 185–205 (2005).
21. L. Breiman, "Random forests," *Mach. Learn.* **45**(1), 5–32 (2001).
22. G. Biau, L. Devroye, and G. Lugosi, "Consistency of random forests and other averaging classifiers," *J. Mach. Learn. Res.* **9**(1), 2015–2033 (2008).
23. G. J. Ughi et al., "Automatic three-dimensional registration of intravascular optical coherence tomography images," *J. Biomed. Opt.* **17**(2), 026005 (2012).
24. H. Peng, "mRMR (minimum redundancy maximum relevance feature selection)," <http://penglab.janelia.org/proj/mRMR/> (March 2013).
25. A. Nair et al., "Automated coronary plaque characterisation with intravascular ultrasound backscatter: ex vivo validation," *EuroIntervention* **3**(1), 113–120 (2007).
26. C. E. Metz, "Basic principles of ROC analysis," *Semin. Nucl. Med.* **8**(4), 283–298 (1978).
27. C. Xu et al., "Characterization of atherosclerosis plaques by measuring both backscattering and attenuation coefficients in optical coherence tomography," *J. Biomed. Opt.* **13**(3), 034003 (2008).
28. G. van Soest et al., "Atherosclerotic tissue characterization in vivo by optical coherence tomography attenuation imaging," *J. Biomed. Opt.* **15**(1), 011105 (2010).
29. A. Bosch, A. Zisserman, and X. Muoz, "Image classification using random forests and ferns," in *IEEE 11th Int. Conf. on Computer Vision*, pp. 1–8, IEEE (2007).
30. T. G. van Leeuwen, D. J. Faber, and M. C. Aalders, "Measurement of the axial point spread function in scattering media using single-mode fiber-based optical coherence tomography," *IEEE J. Sel. Top. Quant. Electr.* **9**(2), 227–233 (2003).
31. G. J. Ughi et al., "Fully automatic three-dimensional visualization of intravascular optical coherence tomography images: methods and feasibility in vivo," *Biomed. Opt. Express* **3**(12), 3291–3303 (2012).